AGU PUBLICATIONS

Geophysical Research Letters

RESEARCH LETTER
10.1002/2016GL067847

Key Points:
- Oceanic barotropization and inverse energy cascade are found at high latitudes
- The energy-containing and conversion scales follow the Rhines and most unstable scales, respectively
- Supercriticality and stratification affect the barotropization and inverse energy cascade

Correspondence to:
R. Chemke,
rei.chemke@weizmann.ac.il

Citation:
Chemke, R., and Y. Kaspi (2016), The latitudinal dependence of the oceanic barotropic eddy kinetic energy and macroturbulence energy transport, *Geophys. Res. Lett.*, *43*, 2723–2731, doi:10.1002/2016GL067847.

Received 17 JAN 2016
Accepted 29 FEB 2016
Accepted article online 4 MAR 2016
Published online 19 MAR 2016

The latitudinal dependence of the oceanic barotropic eddy kinetic energy and macroturbulence energy transport

R. Chemke[1] and Y. Kaspi[1]

[1]Department of Earth and Planetary Sciences, Weizmann Institute of Science, Rehovot, Israel

Abstract Geostrophic turbulence theory predicted already a few decades ago an inverse energy cascade in the barotropic mode, yet there has been limited evidence for it in the ocean. In this study, the latitudinal behavior of the oceanic barotropic energy balance and macroturbulent scales is studied using the ECCO2 (Estimating the Circulation and Climate of the Ocean) state estimate, which synthesizes satellite data and in situ measurements with a high-resolution general circulation model containing realistic bathymetry and wind forcing. It is found that inverse energy cascade occurs at high latitudes, as eddy-eddy interactions spread the conversion of eddy kinetic energy from the baroclinic to the barotropic mode, both upscale and downscale. At these latitudes, the conversion scale of baroclinic eddy kinetic energy and the energy-containing scale follow the most unstable and Rhines scales, respectively. Even though an inverse energy cascade occurs at high latitudes, the energy spectrum follows a steeper slope than the −5/3 slope. Different than classic arguments, the Rossby deformation radius does not follow the baroclinic conversion and most unstable scales.

1. Introduction

The study of oceanic eddies within the framework of two-dimensional turbulence is key for understanding oceanic large-scale turbulent flow (macroturbulence) and the mechanisms controlling the ocean dynamics. Even though baroclinic processes, involving vortex stretching, are one of the most important energy sources in the ocean [*Ferrari and Wunsch*, 2009; *Chen et al.*, 2014], *Charney* [1971] suggested that flow properties of geostrophic turbulence in the atmosphere and ocean resemble that of two-dimensional turbulence. Two prominent features of two-dimensional turbulence are the inverse energy cascade and forward enstrophy cascade [*Fjortoft*, 1953]. These features have a clear signature in the energy spectrum, following a $k^{-5/3}$ and a k^{-3} spectral slope in the inverse energy cascade and forward enstrophy cascade regimes, respectively [*Kraichnan*, 1967]. As energy cascades to larger scales, it cannot keep accumulating; thus, a large-scale dissipation process, such as bottom drag, is required [e.g., *Rivera and Wu*, 2000; *Scott*, 2001; *Smith and Vallis*, 2002; *Danilov and Gurarie*, 2002; *Grianik et al.*, 2004; *Vallis*, 2006; *Tsang and Young*, 2009].

The Rhines-Salmon phenomenology [*Rhines*, 1977; *Salmon*, 1978] incorporated the behavior of two-dimensional turbulence in the energy cycle of geostrophic turbulence. According to this theory the baroclinic flow behaves as a passive tracer, advected by the barotropic flow, and once barotropization occurs, the barotropic flow behaves as in two-dimensional turbulence, with an inverse energy cascade and a forward enstrophy cascade. The barotropization of the flow occurs at the Rossby deformation radius [*Salmon*, 1978; *Smith and Vallis*, 2001], which under baroclinic instability follows the most unstable scale that linear theory predicts [*Eady*, 1949]. As long as friction does not play a major role in the balance [*Danilov and Gurarie*, 2002], the inverse energy cascade in the barotropic mode is halted at the Rhines scale, where the turbulent regime changes to a Rossby wave regime [*Rhines*, 1975]. Thus, in the presence of an inverse energy cascade, the Rhines and energy-containing scales should coincide [*Holloway and Hendershott*, 1977; *Vallis and Maltrud*, 1993; *Held and Larichev*, 1996; *Danilov and Gurarie*, 2000; *Chemke and Kaspi*, 2015].

Even though the vertical structure of the ocean is more complicated than the two-layer phenomenology of *Salmon* [1978], previous studies have found that most of the energy resides in the first baroclinic and barotropic modes [*Wunsch*, 1997; *Fu and Flierl*, 1980; *Smith and Vallis*, 2001; *Ferrari and Wunsch*, 2010; *Venaille et al.*, 2011]. Furthermore, under oceanic like stratification, most of the barotropization occurs from the first baroclinic mode [*Fu and Flierl*, 1980; *Smith and Vallis*, 2001]. The classic two-layer phenomenology does also not account for bottom topography, which plays an important role in the energy balance and vorticity

equation [*Bretherton and Haidvogel*, 1976; *Hughes and Killworth*, 1995; *Ferrari and Wunsch*, 2009], and can even divert the vertical structure of the flow from following the Rhines-Salmon phenomenology [*Arbic and Flierl*, 2004; *Thompson and Young*, 2007].

Using high-resolution satellite data, there has been an extensive effort to understand the energy spectral fluxes at the ocean surface [e.g., *Scott and Wang*, 2005; *Schlösser and Eden*, 2007; *Bühler et al.*, 2014; *Klocker and Abernathey*, 2014]. As these fluxes mostly represent the first baroclinic mode [*Wunsch*, 1997], *Stammer* [1997] argued using altimetric data that the energy-containing scale at the surface follows the first deformation radius. *Scott and Wang* [2005] found an inverse energy cascade at the ocean surface, which differs from the forward cascade in the first baroclinic mode in the Rhines-Salmon phenomenology. Several modeling studies have verified this finding [*Schlösser and Eden*, 2007; *Scott and Arbic*, 2007].

Different than these studies, here we focus on understanding the behavior of the energy fluxes in the barotropic mode. The high-resolution modern state estimate provides an opportunity to examine our understanding of the energy cycle in the barotropic mode in the ocean. While previous studies investigated the barotropic mode using models [e.g., *Fu and Flierl*, 1980; *Smith and Vallis*, 2001; *Venaille et al.*, 2011], the high-resolution ECCO2 data synthesizes our best physical understanding of the ocean with observations. Thus, in this study the theoretical geostrophic turbulence picture can be more realistically examined, as more realistic components (e.g., bottom topography and wind forcing) are taken into account. The global coverage of the ECCO2 also allows studying the barotropic spectral fluxes as a function of latitude. The latitudinal dependence found using the ECCO2 in this study, which shows "classic" barotropic behavior only at high latitudes, was found recently to occur as well in atmospheric general circulation model (GCM) simulations [*Chemke and Kaspi*, 2015].

2. Methodology

In this study, we investigate the oceanic barotropic mode averaged through 23 years (1992–2014) using the Cube92 version of the ECCO2 state estimate, averaged every 3 days. The ECCO2 synthesizes a high-resolution global ocean (0.25° × 0.25° with 50 vertical layers of thicknesses varying from 10 m at the top to approximately 450 m at the bottom), and sea ice configuration [*Zhang et al.*, 1998] of the Massachusetts Institute of Technology ocean GCM [*Marshall et al.*, 1997], with the available satellite (sea surface temperature and height) and in situ (vertical profiles of temperature and salinity) data. The primitive equations for the ocean are solved on a cube-sphere grid projection [*Adcroft et al.*, 2004] with bathymetry [*Menemenlis et al.*, 2008]. A Green function method is used to minimize the misfits between the GCM and observations [*Menemenlis et al.*, 2005]. The solution of the governing equations is constrained to observations by adjusting several control parameters based on the model-data misfit. The partial-cell formulation [*Adcroft et al.*, 1997] is used to account for the discontinuity of the bathymetry.

For calculating the energy spectrum and spectral fluxes in the barotropic mode, a 2-D Fourier decomposition is implemented on 43 land-free regions with 96 grid points in the zonal direction (i.e., 23.75° wide) and with the same width in the meridional direction (Figure 1). While smaller regions do not entirely capture the energy-containing scale, larger regions do not add information for the scale analysis discussed in this paper. As discussed in *Scott and Wang* [2005], even though the ocean does not have periodic boundary conditions, assumed for the Fourier analysis, the results are robust over different region sizes. Similar to *Scott and Wang* [2005] and *Schlösser and Eden* [2007] a Hamming window is applied prior to the Fourier decomposition, and the resulted data are smoothed with a 20-point running mean. As the strongest spatial variations of the barotropic mode occur in the meridional direction, the longitudinal variations of the barotropic mode are beyond the scope of this paper, and unless otherwise stated, the analysis is implemented on each region and the results show their zonal mean.

The spectrum of the barotropic eddy kinetic energy (EKE) is calculated as follows

$$\mathrm{bEKE}_K = \left\langle \left|[u]'_K\right|^2 + \left|[v]'_K\right|^2 \right\rangle , \tag{1}$$

where u and v are the zonal and meridional velocities, angle brackets denote a time mean, squared brackets denote a vertical average, and prime denotes the deviation from zonal mean of each region. The subscript K denotes the spectral components with a total horizontal wave number $K = \sqrt{k_x^2 + k_y^2}$ (wavelength, $L = K^{-1}$),

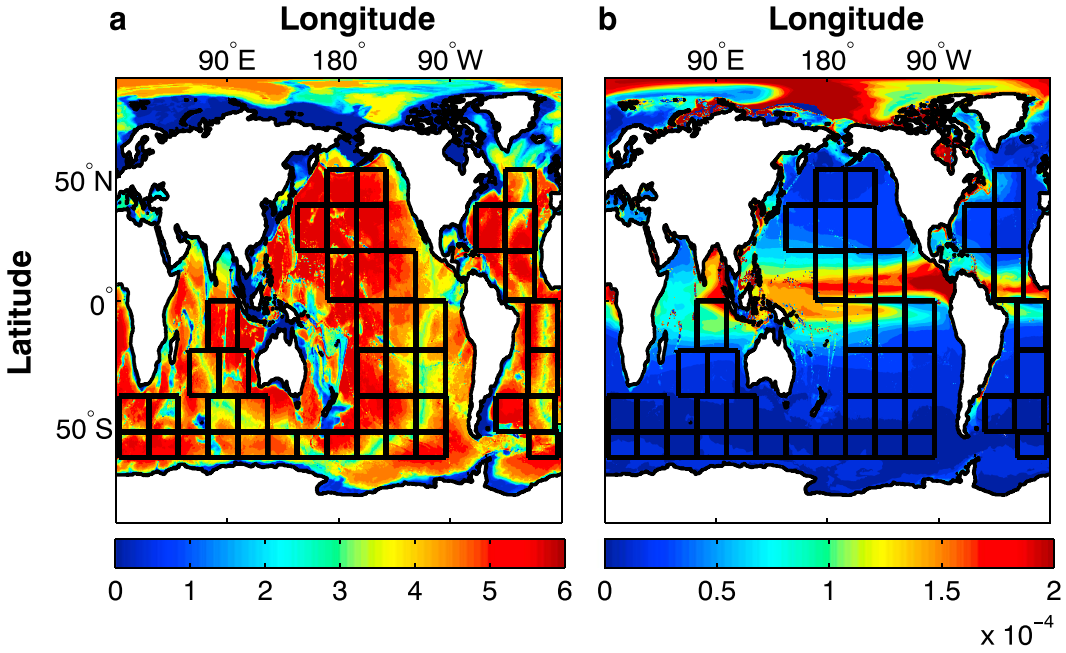

Figure 1. (a) The bathymetry of the ocean (km) and (b) the mean static stability (s^{-2}, see text for definition). The black boxes show the regions used for the analysis.

where k_x and k_y are the zonal and meridional wave numbers, respectively. For studying the eddy behavior in the barotropic mode, each field is first vertically averaged prior to the computation of the deviation from zonal mean. Two components of the barotropic EKE tendency equation are studied here: the conversion of baroclinic to barotropic EKE

$$\mathrm{CT} = \left\langle -[\mathbf{u_h}]_K'^{*} \cdot \left[\mathbf{u}^{+} \cdot \boldsymbol{\nabla}\mathbf{u_h}^{+}\right]_K' \right\rangle \tag{2}$$

and the nonlinear eddy-eddy interactions

$$\mathrm{EE} = \left\langle -[\mathbf{u_h}]_K'^{*} \cdot \left([\mathbf{u}]' \cdot \nabla[\mathbf{u_h}]'\right)_K \right\rangle, \tag{3}$$

where $\mathbf{u}$ denotes the three-dimensional velocity vector, * denotes a complex conjugate, the subscript h denotes the horizontal components of the vector, and $^+$ denotes deviation from vertical average. Equations (2) and (3) are calculated in spherical coordinates.

3. Barotropization at High Latitudes

Although the fundamental theory of geostrophic turbulence [*Rhines*, 1977; *Salmon*, 1978; *Fu and Flierl*, 1980] was found to be suitable for QG two-layer models [e.g., *Larichev and Held*, 1995] and continually stratified models [e.g., *Smith and Vallis*, 2001, 2002], the barotropic behavior of the flow shows a strong latitudinal dependence in GCMs [*Venaille et al.*, 2011; *Chemke and Kaspi*, 2015]. The ECCO2 analysis reveals a similar latitudinal behavior in the ocean (Figure 2). The barotropization of the flow (conversion of baroclinic to barotropic EKE) mostly occurs at high latitudes, poleward of 40° (Figure 2a), with a corresponding inverse energy cascade by eddy-eddy interactions at these latitudes (Figure 2b). Note that different than the two-layer phenomenology [e.g., *Salmon*, 1978; *Larichev and Held*, 1995], here the conversion from baroclinic to barotropic may involve multiple baroclinic modes and not only the first baroclinic mode.

What causes the barotropization of the flow to be more pronounced at high latitudes? The factors that mostly affect barotropization processes according to the scaling theory of *Held and Larichev* [1996], in addition to bottom topography, are the root-mean-square (RMS) barotropic velocity (U_{rms}), the Coriolis parameter (f) and its meridional derivative (β), the stratification (N^2), and zonal shear (u_z). Several studies showed that bottom friction inhibits the barotropization of the flow and weakens the barotropic inverse energy cascade [*Treguier and Hua*, 1988; *Smith and Vallis*, 2002; *Arbic and Flierl*, 2004; *Arbic et al.*, 2007; *Scott and Arbic*, 2007;

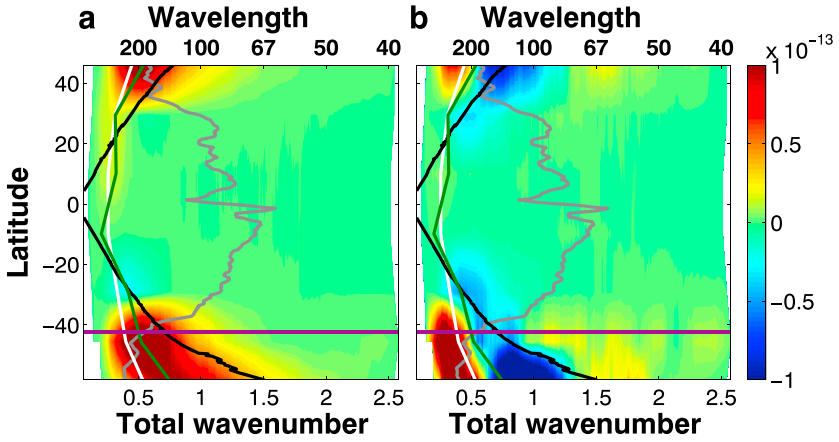

Figure 2. Components of the barotropic EKE equation ($m^2\ s^{-3}$, equations (2) and (3)) as a function of latitude and total wave number ($10^{-5}\ m^{-1}$) and wavelength (km). (a) Conversion from baroclinic EKE to barotropic EKE divided by 5. (b) Transfer of barotropic EKE by eddy-eddy interactions. The black, gray, green, and white lines are the Rossby $\left(K_d = (2\pi L_d)^{-1}\right)$, Rhines $\left(K_\beta = (2\pi L_\beta)^{-1}\right)$, conversion ($K_g$), and energy-containing (K_e) wave numbers, respectively. The purple line shows the latitude where poleward (equatorward) of it the quasi-geostrophic (QG) supercriticality is larger (smaller) than 1. The white areas represent unresolved large and small scales at different latitude bands. Each component is multiplied by the wave number.

Venaille et al., 2011]. However, as steep bottom topography exists through all latitudes (Figure 1a), while the strongest barotropization occurs at high latitudes, particularly in the southern ocean (Figure 2a), bottom topography does not explain the strong barotropization of the flow at high latitudes. This can be further seen by comparing the dependence of barotropization (B_t, calculated as the maximum conversion of baroclinic to barotropic EKE) on bathymetry variance (B_v) through all regions (Figure 3a). Even though an inverse relation between barotropization and bathymetry variance might be expected, the variations in bathymetry have a low effect on barotropization, with even a small tendency to increase it ($B_t \propto B_v^{0.83}$, Figure 3a). Nonetheless, bottom topography may still play a significant role in the balance, as the spatial [*Beckmann et al.*, 1994; *Böning et al.*, 1996; *Smith et al.*, 2000; *Jansen and Held*, 2014] and vertical resolutions at depth (section 2), and the different parameterizations of bottom drag [*Rivière et al.*, 2004; *Thompson and Young*, 2006; *Arbic and Scott*, 2008], may affect both the dissipation of energy and the stratification of the flow.

Previous studies showed that similar to bottom topography, near-surface stratification also tends to weaken the barotropization [*Fu and Flierl*, 1980; *Smith and Vallis*, 2001, 2002]. While uniform stratification results in an efficient barotropization from all baroclinic modes, nonuniform stratification results in energy transfers from high baroclinic modes to the first mode and from there inefficiently to the barotropic mode. Figure 1b shows the mean stratification of the water column above the pycnocline, calculated using the static stability, $N^2 = \frac{g}{\rho_0}\frac{\partial \rho_\theta}{\partial z}$, following *Chelton et al.* [1998], where g is gravity, ρ_0 is background density, and ρ_θ is the potential density. The strongest stratification occurs at low latitudes, while it is weaker and hence more uniform at high latitudes. The strong barotropization at high latitudes may imply that its latitudinal variation is affected by the stratification (Figure 2a). As the largest stratification occurs near the ocean surface, its latitudinal variations are less affected by bottom topography. By comparing the dependence of barotropization (B_t), on stratification (N^2), the stratification clearly decreases the barotropization ($B_t \propto N^{-2.4}$, Figure 3b).

Similar to the barotropization, the U_{rms} (defined as $\mathrm{bEKE}^{0.5}$) is also larger at high latitudes. Large values of barotropic EKE may imply a stronger energy cycle at these latitudes. The barotropic EKE indeed tends to increase the barotropization ($B_t \propto \mathrm{bEKE}^{0.93}$, Figure 3c). The vertical shear of the zonal flow also weakly increases the barotropization, but it is not statistically significant ($B_t \propto u_z^{0.8}$, Figure 3d). The sphericity parameters (the Coriolis parameter and its meridional derivative), on the other hand, may also explain the latitudinal dependence of the barotropization, as the Coriolis parameter and the β effect tend to increase and decrease the barotropization of the flow, respectively ($B_t \propto f^2\beta^{-5.3}$, Figures 3e and 3f). Thus, the main factors affecting the latitudinal variations of the barotropization are the stratification, sphericity of the planet, and barotropic EKE.

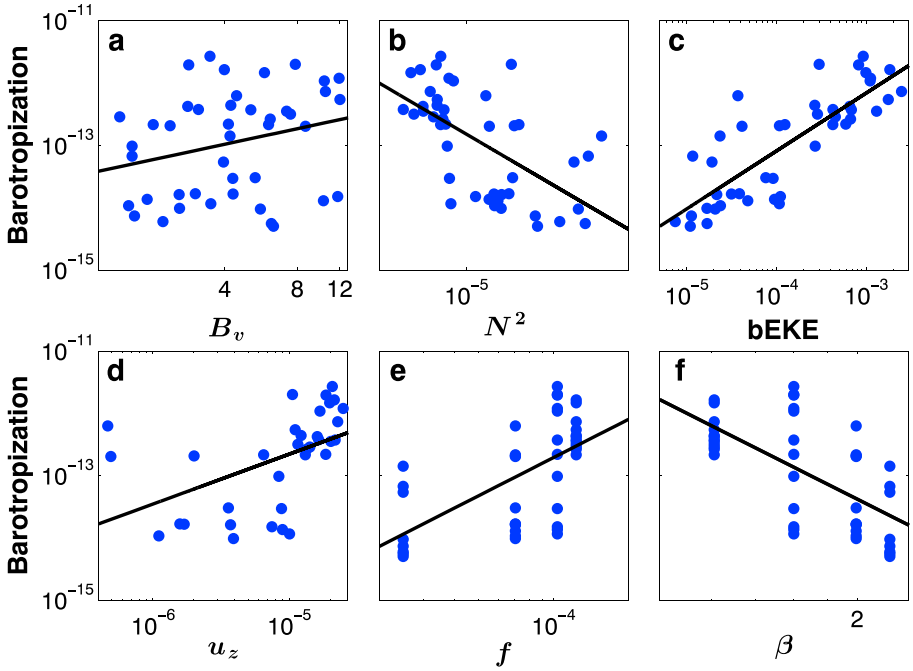

Figure 3. Maximum baroclinic to barotropic EKE conversion (B_t, $m^2\ s^{-3}$) at each region presented in Figure 1 as a function of (a) the variance of bathymetry (B_v, 10^5 m), (b) the mean static stability (N^2, s^{-2}), (c) the barotropic eddy kinetic energy (bEKE, $m^2\ s^{-2}$), (d) the vertical shear of the zonal flow (u_z, s^{-1}), and (f) the meridional derivative of the Coriolis parameter (β, $10^{-11}\ m^{-1}\ s^{-1}$). The black lines represent the best fits and follow 0.83 ± 0.96 ($R^2 = 0.068$), -1.2 ± 0.4 ($R^2 = 0.36$), 0.93 ± 0.2 ($R^2 = 0.67$), 0.8 ± 0.2 ($R^2 = 0.24$), 2 ± 0.8 ($R^2 = 0.36$), and -5.3 ± 2 ($R^2 = 0.4$) slopes in Figures 3a–3f, respectively, where the errors represent the 95% confidence interval.

4. Barotropic Inverse Energy Cascade

The strong barotropization at high latitudes does not necessarily ensure a barotropic inverse energy cascade at these latitudes. For an inverse energy cascade to occur, there must be a scale separation between the conversion scale of baroclinic to barotropic EKE and the energy-containing scale [*Salmon*, 1978]. Indeed, the inverse energy cascade at high latitudes (Figure 2b) is consistent with a scale separation between the conversion wave number of baroclinic to barotropic EKE (K_g, green line in Figure 2) and the energy-containing wave number (K_e, white line in Figure 2). The energy-containing and conversion wave numbers are defined as the wave numbers where the barotropic energy spectrum (equation (1)) and the conversion of baroclinic to barotropic EKE (Figure 2a and equation (2)) are at maximum, respectively. At lower latitudes, the energy-containing wave number and the conversion wave number of baroclinic to barotropic EKE nearly coincide. To better understand the latitudinal dependence of these scales, we now investigate different parameterizations for them.

Different than the classic Rhines-Salmon phenomenology, the region-averaged Rossby deformation wave number does not coincide with the conversion wave number (black and green lines in Figure 2a and red dots in Figure 4a). The Rossby deformation wave number is defined as, $K_d = \left(\lambda_d\right)^{-1}$, where $\lambda_d = 2\pi L_d$ is the Rossby deformation wavelength [*Scott and Wang*, 2005; *Abernathey and Wortham*, 2015] and $L_d = \frac{1}{|f|\pi}\int_0^H N dz$ is the Rossby deformation radius, calculated following *Chelton et al.* [1998], where H is the water column depth. Following *Smith* [2007], we calculate the most unstable wave number $\left(K_m\right)$ by applying a linear normal mode instability analysis on the linearized quasi-geostrophic (QG) potential vorticity equation. Using the region-averaged time mean flow, density, and meridional potential vorticity gradient, the eigenvalues are calculated at each region presented in Figure 1. As discussed in *Smith* [2007], for accounting only the energetically important wave numbers the growth rate is normalized by the eddy available potential energy, which is calculated using the variance of the potential temperature field [e.g., *Lorenz*, 1955; *Saltzman*, 1957; *Boer*, 1975]. The conversion wave number does coincide with the most unstable wave number (similar to *Jansen and Ferrari* [2012] and *Berloff and Kamenkovich* [2013]), through almost all latitudes, except at latitudes near the equator where there may not be baroclinic instability (orange dots, Figure 4b). These results are different than in

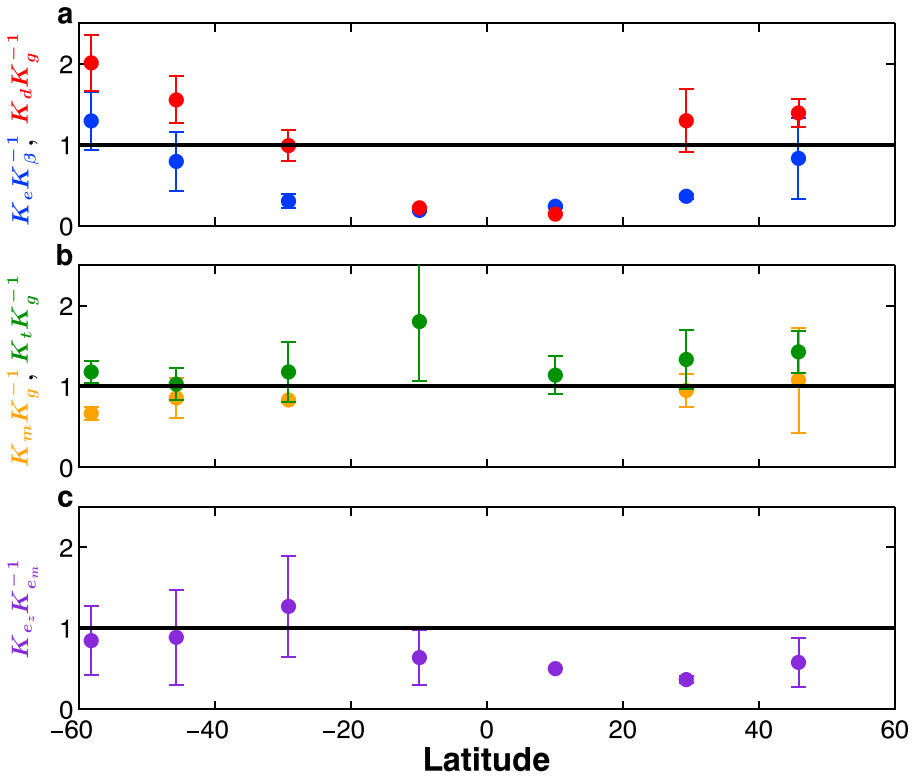

Figure 4. Ratio of macroturbulent scales as a function of latitude. (a) The ratio of the region-averaged Rossby wave number (K_d) and the conversion wave number of baroclinic to barotropic EKE (K_g, red dots), and the ratio of the energy-containing wave number (K_e) and the region-averaged Rhines wave number (K_β, blue dots). (b) The ratio of the most unstable wave number (K_m) and the conversion wave number of baroclinic to barotropic EKE (K_g, orange dots), and the ratio of the transition wave number (K_t) and the conversion wave number of baroclinic to barotropic EKE (K_g, green dots). At the two closest latitudes to the equator the ratios between the most unstable and conversion wave numbers are off the *y* axis limit. (c) The ratio of the zonal $\left(K_{e_z}\right)$ and meridional $\left(K_{e_m}\right)$ energy-containing wave numbers. The error bars represent the standard deviation along each latitudinal band.

Schlösser and Eden [2007], where the deformation radius was found to be proportional to the conversion scale near the ocean surface. In the barotropic mode, on the other hand, at high (low) latitudes the conversion wave number, and hence the most unstable wave number (as was shown by *Venaille et al.* [2011] and *Tulloch et al.* [2011]), is smaller (larger) than the Rossby deformation wave number (red dots, Figure 4a). The congruity of the conversion and the most unstable wave numbers emphasizes the role of baroclinic instability in the barotropization of the flow [*Qiu et al.*, 2008] and may explain the increase of the conversion wave number with latitude (green line in Figure 2a), as the main controlling parameters in baroclinic instability are the Coriolis parameter, stratification, and zonal mean shear [e.g., *Eady*, 1949; *Phillips*, 1954].

In agreement with *Rhines* [1975] and with idealized atmospheric GCM simulations [*Jansen and Ferrari*, 2012; *Chemke and Kaspi*, 2015], only at high latitudes where inverse energy cascade occurs (Figure 2b), indeed, the Rhines wave number, K_β, follows the energy-containing wave number (white and gray lines in Figure 2 and blue dots in Figure 4a). The Rhines wave number is defined as $K_\beta = \left(\lambda_\beta\right)^{-1}$, where $\lambda_\beta = 2\pi L_\beta$ is the Rhines wavelength [*Scott and Wang*, 2005; *Abernathey and Wortham*, 2015], and following *Rhines* [1975], $L_\beta = \left(\frac{2U_{\mathrm{rms}}}{\beta}\right)^{0.5}$ is the Rhines scale. Different than surface observations [e.g., *Stammer*, 1997], here the Rossby deformation wave number does not follow the barotropic energy-containing wave number (black and white lines in Figure 2). Even though this picture differs from the Rhines-Salmon phenomenology, since the conversion wave number does not follow the Rossby deformation wave number, the ratio between the Rhines scale and Rossby deformation radius does predict regions where inverse energy cascade does and does not occur (poleward and equatorward of where the black and gray lines meet in Figure 2).

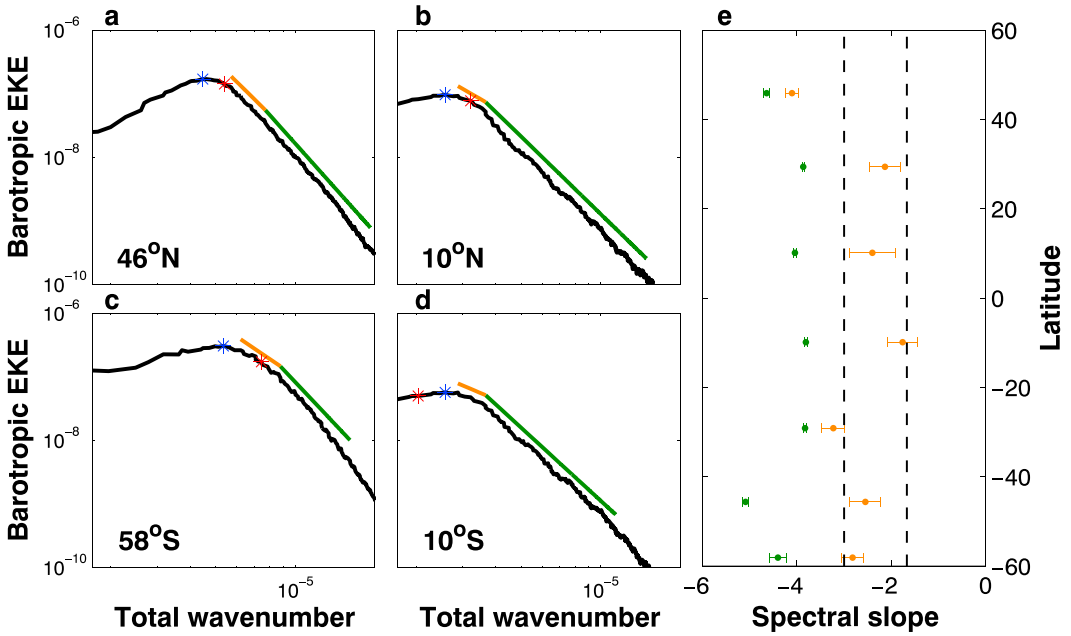

Figure 5. The spectrum of the barotropic EKE ($m^2\ s^{-2}$) as a function of total wave number (m^{-1}) for latitude bands centered at (a) 46°N, (b) 10°N, (c) 58°S, and (d) 10°S. The blue and red asterisks are the energy-containing wave number (K_e) and the conversion wave number of baroclinic to barotropic EKE (K_g), respectively. The orange and green lines are the best linear fit slopes. (e) The spectral slopes as function of latitude with error bars of 95% confidence interval. The two vertical dashed lines correspond to the −5/3 and −3 spectral slopes.

The QG supercriticality was suggested by *Held and Larichev* [1996] to follow the ratio of the Rhines scale and Rossby deformation radius. The horizontal purple line in Figure 2 shows the latitude where the QG supercriticality, $S_c = \frac{f^2 u_z}{\beta H N^2}$, equals 1. While in the southern ocean, values of QG supercriticality larger than 1 do follow latitudes where the Rhines scale is larger than the Rossby deformation radius, and where inverse energy cascade occurs (similar to *Chemke and Kaspi* [2015]), in the northern ocean, on the other hand, values of QG supercriticality are everywhere smaller than 1. At low latitudes, where the QG supercriticality is smaller than 1 and the inverse energy cascade is inhibited (Figure 2b), the Rhines wave number is larger than the energy-containing wave number (blue dots in Figure 4a). Several studies showed the presence of a more isotropic regime, governed by eddies, poleward of the latitude where the Rhines scale is larger than the Rossby deformation radius, while equatorward of this latitude is a more wave regime [*Theiss*, 2004; *Chelton et al.*, 2007; *Eden*, 2007; *Sayanagi et al.*, 2008; *Klocker and Abernathey*, 2014]. The ratio between the barotropic energy-containing zonal and meridional wave numbers does show mild evidence for more zonally elongated eddies at low latitudes and more isotropic flow at high latitudes (Figure 4c).

Bottom drag has also been found to decrease the energy-containing scale [*Smith and Vallis*, 2002; *Arbic and Flierl*, 2004; *Thompson and Young*, 2007]. The energy-containing scale decreases at high latitudes in both hemispheres (white line Figure 2); however, strong topographic variations occur through all latitudes. Bottom topography could also decrease the inverse energy cascade strength [*Treguier and Hua*, 1988; *Scott and Arbic*, 2007]. In the southern ocean, however, where bottom topography might play an important role [*Wunsch and Ferrari*, 2004; *Masich et al.*, 2015], the inverse cascade is largest (Figure 2b). Thus, in spite the dominant bottom topography, the presence of strong inverse energy cascade at high latitudes, in both hemispheres, suggests the importance of the supercriticality (the sphericity parameters, stratification, and vertical shear) in affecting the inverse cascade [*Smith and Vallis*, 2002], through the scale separation of the conversion scale (baroclinic instability) and the energy-containing scale (the Rhines effect). Again, care should be taken before ignoring the effects of bottom drag, as it may be subjected to the parameterization [*Arbic and Scott*, 2008] and the coarse horizontal and vertical (near the ocean floor) resolutions of the model.

5. The Spectrum of the Barotropic EKE

To further analyze the barotropic inverse energy cascade, the spectral slopes of the barotropic EKE (equation (1)) are calculated and shown in Figure 5. The spectral slopes are calculated in log-log space at each region using a linear least squares fit algorithm, applied to find the best (largest coefficient of determination) one or two slopes for the energy spectrum, beyond the roll-off of the spectrum near the energy-containing wave number (K_e) and down to 1.2×10^{-5} m^{-1} in order to avoid fitting submesoscales. Different than the conversion of EKE from baroclinic to barotropic and the inverse energy cascade by eddy-eddy interactions (Figure 2), which intensify with latitude, the spectral slopes do not show such latitudinal behavior (Figure 5).

Following the classic arguments of 2-D turbulence [*Kraichnan*, 1967], we expect to find at large-scales of the spectrum the −5/3 slope, only at latitudes where inverse energy cascade is observed (Figure 2b). However, steeper slopes than −5/3 appear through almost all latitudes, especially at high latitudes (Figure 5e). *Larichev and Held* [1995] suggested that a broad input of baroclinic energy to the barotropic mode at large-scales could affect the spectral slopes. This might explain the steeper slopes, as the conversion of baroclinic to barotropic does not occur at a specific scale, but rather through a wide range of scales (Figure 2a). The spectral slope at small scales follows a −4 slope through all latitudes, which is steeper than −3 slopes of forward enstrophy cascade in 2-D turbulence [*Kraichnan*, 1967], likely due to dissipation processes at small scales. Near the grid scale the forward energy cascade in Figure 2b may be an artifact of the coarse resolution [*Jansen and Held*, 2014]. The transition wave number (K_t, the wave number where the slope changes discontinuously in Figures 5a–5d, where the two best fit segments meet) coincides with the conversion wave number of baroclinic to barotropic EKE, mostly in the southern ocean (red asterisk in Figure 5 and green dots in Figure 4b). This again emphasizes that the energy source for the different behavior at small (inverse energy cascade) and large (forward enstrophy cascade) wave numbers is likely related to baroclinic instability.

Acknowledgments
We thank Matthew Mazloff, Eli Tziperman, and Janni Yuval for very fruitful discussions during the preparation of this manuscript. We would also like to thank Malte Jansen and an anonymous reviewer whose comments have helped to improve the manuscript. Data have been provided by the ECCO2 project: ftp://ecco2.jpl.nasa.gov/data1/cube/cube92/lat_lon/quart_90S_90N/. This research has been supported by an EU-FP7 Marie Curie Career Integration Grant (CIG-304202), the Israeli Science Foundation (grant 1310/12), and the Israeli Ministry of Science.

References

Abernathey, R., and C. Wortham (2015), Phase speed cross spectra of eddy heat fluxes in the Eastern Pacific, *J. Phys. Oceanogr.*, *45*, 1285–1301.
Adcroft, A., C. Hill, and J. Marshall (1997), Representation of topography by shaved cells in a height coordinate ocean model, *Mon. Weather Rev.*, *125*, 2293–2315.
Adcroft, A., J.-M. Campin, C. Hill, and J. Marshall (2004), Implementation of an atmosphere-ocean general circulation model on the expanded spherical cube, *Mon. Weather Rev.*, *132*, 2845–2863.
Arbic, B. K., and G. R. Flierl (2004), Baroclinically unstable geostrophic turbulence in the limits of strong and weak bottom Ekman friction: Application to midocean eddies, *J. Phys. Oceanogr.*, *34*, 2257–2273.
Arbic, B. K., and R. B. Scott (2008), On quadratic bottom drag, geostrophic turbulence, and oceanic mesoscale eddies, *J. Phys. Oceanogr.*, *38*, 84–103.
Arbic, B. K., G. R. Flierl, and R. B. Scott (2007), Cascade inequalities for forced-dissipated geostrophic turbulence, *J. Phys. Oceanogr.*, *37*(6), 1470–1487.
Beckmann, A., C. W. Böning, C. Köberle, and J. Willebrand (1994), Effects of increased horizontal resolution in a simulation of the North Atlantic Ocean, *J. Phys. Oceanogr.*, *24*, 326–344, doi:10.1175/1520-0485(1994)024<0326:EOIHRI>2.0.CO;2.
Berloff, P., and I. Kamenkovich (2013), On spectral analysis of mesoscale eddies. Part II: Nonlinear analysis, *J. Phys. Oceanogr.*, *43*, 2528–2544.
Boer, G. J. (1975), Zonal and eddy forms of the available potential energy equations in pressure coordinates, *Tellus*, *27*(5), 433–442.
Böning, C. W., F. O. Bryan, W. R. Holland, and R. Döscher (1996), Deep-water formation and meridional overturning in a high-resolution model of the North Atlantic, *J. Phys. Oceanogr.*, *26*, 1142–1164, doi:10.1175/1520-0485(1996)026<1142:DWFAMO>2.0.CO;2.
Bretherton, F. P., and D. B. Haidvogel (1976), Two-dimensional turbulence above topography, *J. Fluid Mech.*, *78*, 129–154.
Bühler, O., J. Callies, and R. Ferrari (2014), Wave-vortex decomposition of one-dimensional ship-track data, *J. Fluid Mech.*, *756*, 1007–1026.
Charney, J. G. (1971), Geostrophic turbulence, *J. Atmos. Sci.*, *28*(6), 1087–1095.
Chelton, D. B., R. A. Deszoeke, M. G. Schlax, E. Naggar, and N. Siwertz (1998), Geographical variability of the first baroclinic Rossby radius of deformation, *J. Phys. Oceanogr.*, *28*(3), 433–460.
Chelton, D. B., M. G. Schlax, R. M. Samelson, and R. A. de Szoeke (2007), Global observations of large oceanic eddies, *Geophys. Res. Lett.*, *34*, L15606, doi:10.1029/2007GL030812.
Chemke, R., and Y. Kaspi (2015), The latitudinal dependence of atmospheric jet scales and macroturbulent energy cascades, *J. Atmos. Sci.*, *72*(10), 3891–3907.
Chen, R., G. R. Flierl, and C. Wunsch (2014), A description of local and nonlocal eddy-mean flow interaction in a global eddy-permitting state estimate, *J. Phys. Oceanogr.*, *44*, 2336–2352.
Danilov, S., and D. Gurarie (2002), Rhines scale and spectra of the beta plane turbulence with bottom drag, *Phys. Rev. E*, *65*(6), 067301.
Danilov, S. D., and D. Gurarie (2000), Quasi-two-dimensional turbulence, *Usp. Fiz. Nauk*, *170*(9), 921–968.
Eady, E. T. (1949), Long waves and cyclone waves, *Tellus*, *1*(3), 33–52.
Eden, C. (2007), Eddy length scales in the North Atlantic Ocean, *J. Geophys. Res.*, *112*, C06004, doi:10.1029/2006JC003901.
Ferrari, R., and C. Wunsch (2009), Ocean circulation kinetic energy: Reservoirs, sources, and sinks, *Ann. Rev. Fluid Mech.*, *41*, 253–282.
Ferrari, R., and C. Wunsch (2010), The distribution of eddy kinetic and potential energies in the global ocean, *Tellus*, *62*, 92–108.
Fjortoft, R. (1953), On the changes in the spectral distribution of kinetic energy for twodimensional, nondivergent flow, *Tellus*, *5*(3), 225–230.
Fu, L.-L., and G. R. Flierl (1980), Nonlinear energy and enstrophy transfers in a realistically stratified ocean, *Dyn. Atmos. Oceans*, *4*(4), 219–246.
Grianik, N., I. M. Held, K. S. Smith, and G. K. Vallis (2004), The effects of quadratic drag on the inverse cascade of two-dimensional turbulence, *Phys. Fluids*, *16*(1), 73–78.

Held, I. M., and V. D. Larichev (1996), A scaling theory for horizontally homogeneous, baroclinically unstable flow on a beta plane, *J. Atmos. Sci.*, *53*(7), 946–952.
Holloway, G., and M. C. Hendershott (1977), Stochastic closure for nonlinear Rossby waves, *J. Fluid Mech.*, *82*(4), 747–765.
Hughes, C. W., and P. D. Killworth (1995), Effects of bottom topography in the large-scale circulation of the Southern Ocean, *J. Phys. Oceanogr.*, *25*, 2485–2497.
Jansen, M., and R. Ferrari (2012), Macroturbulent equilibration in a thermally forced primitive equation system, *J. Atmos. Sci.*, *69*(2), 695–713.
Jansen, M. F., and I. M. Held (2014), Parameterizing subgrid-scale eddy effects using energetically consistent backscatter, *Ocean Modell.*, *80*, 36–48.
Klocker, A., and R. Abernathey (2014), Global patterns of mesoscale eddy properties and diffusivities, *J. Phys. Oceanogr.*, *44*(3), 1030–1046.
Kraichnan, R. H. (1967), Inertial ranges in two-dimensional turbulence, *Phys. Fluids*, *10*, 1417–1423.
Larichev, V. D., and I. M. Held (1995), Eddy amplitudes and fluxes in a homogeneous model of fully developed baroclinic instability, *J. Phys. Oceanogr.*, *25*(10), 2285–2297.
Lorenz, E. N. (1955), Available potential energy and the maintenance of the general circulation, *Tellus*, *7*(2), 157–167.
Marshall, J., A. Adcroft, C. Hill, L. Perelman, and C. Heisey (1997), Hydrostatic, quasi-hydrostatic, and nonhydrostatic ocean modeling, *J. Geophys. Res.*, *102*(C3), 5733–5752.
Masich, J., T. K. Chereskin, and M. R. Mazloff (2015), Topographic form stress in the Southern Ocean state estimate, *J. Geophys. Res. Oceans*, *120*, 7919–7933, doi:10.1002/2015JC011143.
Menemenlis, D., I. Fukumori, and T. Lee (2005), Using Green's functions to calibrate an ocean general circulation model, *Mon. Weather Rev.*, *133*, 1224–1240.
Menemenlis, D., J. Campin, P. Heimbach, C. Hill, T. Lee, A. Nguyen, M. Schodlok, and H. Zhang (2008), ECCO2: High resolution global ocean and sea ice data synthesis, *Mercator Ocean Q. Newsl.*, *31*, 13–21.
Phillips, N. A. (1954), Energy transformations and meridional circulations associated with simple baroclinic waves in a two level quasi-geostrophic model, *Telus*, *6*(3), 273–286.
Qiu, B., R. B. Scott, and S. Chen (2008), Length scales of eddy generation and nonlinear evolution of the seasonally modulated South Pacific subtropical countercurrent, *J. Phys. Oceanogr.*, *38*, 1515–1528.
Rhines, P. B. (1975), Waves and turbulence on a beta plane, *J. Fluid Mech.*, *69*(03), 417–443.
Rhines, P. B. (1977), The dynamics of unsteady currents, *Sea*, *6*, 189–318.
Rivera, M., and X. L. Wu (2000), External dissipation in driven two-dimensional turbulence, *Phys. Rev. Let.*, *85*(5), 976.
Rivière, P., A. M. Treguier, and P. Klein (2004), Effects of Bottom friction on nonlinear equilibration of an oceanic baroclinic jet, *J. Phys. Oceanogr.*, *34*, 416–432.
Salmon, R. (1978), Two-layer quasi-geostrophic turbulence in a simple special case, *Geophys. Astrophys. Fluid Dyn.*, *10*(1), 25–52.
Saltzman, B. (1957), Equations governing the energetics of the larger scales of atmospheric turbulence in the domain of wave number, *J. Meteorol.*, *14*(6), 513–523.
Sayanagi, K. M., A. P. Showman, and T. E. Dowling (2008), The emergence of multiple robust zonal jets from freely evolving, three-dimensional stratified geostrophic turbulence with applications to Jupiter, *J. Atmos. Sci.*, *65*(12), 3947–3962.
Schlösser, F., and C. Eden (2007), Diagnosing the energy cascade in a model of the North Atlantic, *Geophys. Res. Lett.*, *34*, L02604, doi:10.1029/2006GL027813.
Scott, R. B. (2001), Evolution of energy and enstrophy containing scales in decaying, two-dimensional turbulence with friction, *Phys. Fluids*, *13*(9), 2739–2742.
Scott, R. B., and B. K. Arbic (2007), Spectral energy fluxes in geostrophic turbulence: Implications for ocean energetics, *J. Phys. Oceanogr.*, *37*(3), 673–688.
Scott, R. B., and F. Wang (2005), Direct evidence of an oceanic inverse kinetic energy cascade from satellite altimetry, *J. Phys. Oceanogr.*, *35*(9), 1650–1666.
Smith, K. S. (2007), The geography of linear baroclinic instability in Earth's oceans, *J. Mar. Res.*, *65*(5), 655–683.
Smith, K. S., and G. K. Vallis (2001), The scales and equilibration of midocean eddies: Freely evolving flow, *J. Phys. Oceanogr.*, *31*(2), 554–571.
Smith, K. S., and G. K. Vallis (2002), The scales and equilibration of midocean eddies: Forced-dissipative flow, *J. Phys. Oceanogr.*, *32*(6), 1699–1720.
Smith, L. T., E. P. Chassignet, and R. Bleck (2000), The impact of lateral boundary conditions and horizontal resolution on North Atlantic water mass transformations and pathways in an isopycnic coordinate ocean model, *J. Phys. Oceanogr.*, *30*, 137–159, doi:10.1175/1520-0485(2000)030<0137:TIOLBC>2.0.CO;2.
Stammer, D. (1997), Global characteristics of ocean variability estimated from regional TOPEX/POSEIDON altimeter measurements, *J. Phys. Oceanogr.*, *27*(8), 1743–1769.
Theiss, J. (2004), Equatorward energy cascade, critical latitude, and the predominance of cyclonic vortices in geostrophic turbulence, *J. Phys. Oceanogr.*, *34*(7), 1663–1678.
Thompson, A. F., and W. R. Young (2006), Scaling baroclinic eddy fluxes: Vortices and energy balance, *J. Phys. Oceanogr.*, *36*, 720–738.
Thompson, A. F., and W. R. Young (2007), Two-layer baroclinic eddy heat fluxes: Zonal flows and energy balance, *J. Phys. Oceanogr.*, *64*, 3214–3231.
Treguier, A. M., and B. L. Hua (1988), Influence of bottom topography on stratified quasi-geostrophic turbulence in the ocean, *Geophys. Astrophys. Fluid Dyn.*, *43*, 265–305.
Tsang, Y. K., and W. R. Young (2009), Forced-dissipative two-dimensional turbulence: A scaling regime controlled by drag, *Phys. Rev. E*, *79*(4), 045308.
Tulloch, R., J. Marshall, C. Hill, and K. S. Smith (2011), Scales, growth rates, and spectral fluxes of baroclinic instability in the ocean, *J. Phys. Oceanogr.*, *41*(6), 1057–1076.
Vallis, G. K. (2006), *Atmospheric and Oceanic Fluid Dynamics*, 745 pp., Cambridge Univ. Press, Cambridge, U. K.
Vallis, G. K., and M. E. Maltrud (1993), Generation of mean flows and jets on a beta plane and over topography, *J. Phys. Oceanogr.*, *23*(7), 1346–1362.
Venaille, A., K. S. Smith, and G. K. Vallis (2011), Baroclinic turbulence in the ocean: Analysis with primitive equation and quasigeostrophic simulations, *J. Phys. Oceanogr.*, *41*(9), 1605–1623.
Wunsch, C. (1997), The vertical partition of oceanic horizontal kinetic energy, *J. Phys. Oceanogr.*, *27*, 1770–1794.
Wunsch, C., and R. Ferrari (2004), Vertical mixing, energy, and the general circulation of the oceans, *Annu. Rev. Fluid Mech.*, *36*, 281–314.
Zhang, J., W. D. Hibler III, M. Steele, and D. A. Rothrock (1998), Arctic ice ocean modeling with and without climate restoring, *J. Phys. Oceanogr.*, *28*, 191–217.